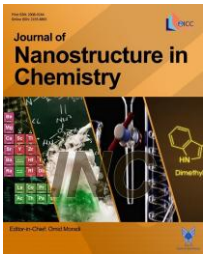

J. Nanostruct Chem. 2026; 16(4): 366-379

Journal of Nanostructure in Chemistry (JNSC)

https://doi.org/10.57647/jnsc.2026.1604.18

Research Article

Ultrasensitive SERS-Active Silver/Graphene Oxide Nanocomposites for Label-Free Detection of Lung Cancer-Associated miRNA-21

Lei Xu[1,2], Jiaru Jiang [3], Li Zhang[4], Sicong Jiang[5], Guangyi Zhang [1,2,*]

[1]*Department of Respiratory and Critical Care Medicine, The First Affiliated Hospital, Jiangxi Medical College, Nanchang University, Nanchang, Jiangxi, 330209, China*

[2]*China-Japan Friendship Jiangxi Hospital, National Regional Center for Respiratory Medicine, Nanchang, Jiangxi, 330200, China*

[3]*Department of Pulmonary and Critical Care Medicine, Loudi Central Hospital, Loudi 417000, China*

[4]*Cadre Health Care Office, The First Affiliated Hospital, Jiangxi Medical College, Nanchang University, 1519 Dongyue Dadao, Nanchang 330006, China*

[5]*Division of Thoracic and Endocrine Surgery, University Hospitals and University of Geneva, Geneva 4,1211, Switzerland*

[*] **Corresponding authors:** ndyfy05902@ncu.edu.cn

Article History:

Received:
25 April 2026

Revised:
09 February 2026

Accepted:
19 January 2026

Published in Issue:
31 August 2026

Abstract

This study reports an ultrasensitive Ag/graphene oxide (Ag/GO) hybrid substrate for label-free SERS detection of lung cancer-associated miRNA-21. Three Ag precursor loadings were evaluated to clarify how metal loading controls nanoparticle density, interparticle spacing, and hot-spot formation. The intermediate formulation, Ag/GO-2, provided the most favorable balance between morphological uniformity and plasmonic coupling, yielding an average Ag crystallite size of about 18.5 nm and an Ag loading of 35.6 wt% by ICP-MS, in good agreement with TGA. A 532 nm laser and 0.5 mW power were selected from a preliminary optimization study to maximize signal stability while minimizing photothermal perturbation of RNA. Using rhodamine 6G as a probe, Ag/GO-2 exhibited an enhancement factor of 2.4 x 10^7. For miRNA-21, the adenine band at 732 cm^{-1} showed a linear response from 10^{-7} to 10^{-13} M ($R^2 = 0.948$) with a limit of detection of 15 fM. Specificity was verified against a single-base mutant, miR-21-3p, let-7a, miR-141, and BSA using full spectral fingerprints and multivariate PCA. The platform showed good spot-to-spot reproducibility (12.4% RSD), acceptable inter-batch reproducibility (<11% RSD), retained more than 85% of its initial activity after 30 days under dark sealed storage, and delivered 92.0-108.0% recovery in 1:10 diluted serum while maintaining detectable signals in 1:2 and undiluted serum. These results clarify the Ag-loading/structure/performance relationship and support the practical potential of Ag/GO substrates for liquid-biopsy-oriented nucleic-acid sensing.

Keywords: Cancer biomarkers; Graphene oxide nanocomposite; Liquid biopsy; Lung cancer-associated miRNA-21; Surface-enhanced Raman spectroscopy

Cite this article: Xu L., Jiang J., Zhang L., Jiang S., Zhang G. Ultrasensitive SERS-Active Silver/Graphene Oxide Nanocomposites for Label-Free Detection of Lung Cancer-Associated miRNA-21. *J Nanostruct Chem* **16**, 366-379 (2026). https://doi.org/10.57647/jnsc.2026.1604.18

1. Introduction

Lung cancer remains the leading cause of cancer-related mortality worldwide [1]. The survival benefit associated with early-stage detection remains substantial [2]. Although low-dose computed tomography has improved screening coverage [3], persistent false positives and patient-safety concerns still limit its value as a standalone molecular screening tool [4]. Conventional tissue biopsy is likewise invasive and samples only a localized portion of a heterogeneous tumor [5]. These limitations have accelerated interest in liquid-biopsy strategies capable of repeatedly interrogating circulating tumor-associated biomarkers in a minimally invasive manner [6]. Among

circulating biomarkers, microRNAs (miRNAs) are especially attractive because they are short, relatively stable in blood, and closely linked to oncogenic regulation. miRNA-21 is one of the most consistently upregulated oncomiRs in non-small cell lung cancer [7]. Its biological and translational relevance in lung-cancer progression has been emphasized in mechanistic studies [8] and biomarker-focused reports [9]. However, analytical translation remains difficult: mature miRNAs are often present at very low abundance, differ from homologous sequences by only one or a few nucleotides, and are vulnerable to adsorption losses, nuclease exposure, and matrix interference during assay handling [10]. RT-qPCR remains the most widely used reference method for miRNA analysis because of its high analytical sensitivity [11], but it depends on reverse transcription, enzymatic amplification, target-specific primers, and tightly controlled thermal cycling. Practical workflow guidance also highlights the burden of assay optimization and normalization in low-copy-number settings [12]. Direct, label-free methods that can read molecular fingerprints without enzymatic amplification therefore remain highly attractive, provided that they can still deliver adequate sensitivity, sequence discrimination, and robustness in biofluids.

Surface-enhanced Raman scattering (SERS) addresses this challenge by coupling analytes to nanostructured plasmonic surfaces that strongly amplify the local electromagnetic field [13] and, in some cases, promote interfacial charge-transfer enhancement. Recent biological-Raman reviews also underline the value of molecular fingerprinting for label-free analysis [14]. When localized surface plasmon resonance is excited in silver or gold nanostructures, electromagnetic hot spots arise preferentially in narrow interparticle gaps, where both the incident and scattered fields are intensified [15]. The hot-spot concept remains central to plasmon-enhanced Raman analysis across nanostructured substrates [16]. Unlike labeled sandwich assays, label-free SERS preserves the intrinsic nucleobase fingerprint of the target oligonucleotide and therefore offers the possibility of direct sequence discrimination from the spectral pattern itself. Besides electromagnetic enhancement, graphene-based supports can contribute chemically by modulating interfacial charge transfer and by enriching nucleic acids near the metal surface. Graphene oxide (GO) provides a large aromatic platform for pi-pi interactions with nucleobases, residual oxygenated groups for Ag anchoring, and improved dispersion relative to bare colloidal Ag nanoparticles. The key materials challenge is to control Ag loading closely enough to create high-density nanogaps without triggering overgrowth, nonuniform aggregation, or rapid signal loss during storage. Several elegant SERS-based miRNA assays have already been reported, including amplification-assisted label-free detection of miR-21 using iodide-modified Ag nanoparticles [17], optofluidic label-free quantification of miRNA on metal-dielectric SERS chips [18], and direct fingerprint-based detection of unlabeled miRNA on silver nanostructures [19]. Nevertheless, many reported strategies still rely on colloidal aggregation, enzymatic amplification, microfluidic functionalization, or substrate architectures that are not straightforward to reproduce in a simple drop-cast workflow. Ag/GO composites remain especially attractive because GO can enrich nucleic acids through pi-pi interactions [20], contribute to interfacial charge-transfer pathways [21], improve SERS stability in Ag/GO composites [22], and support related GO/Ag sensing architectures [23].

Based on this context, we designed an in-situ synthesized Ag/GO platform for direct label-free detection of miRNA-21 and systematically optimized the Ag loading to balance nanoparticle density, nanogap formation, mesoporosity, and colloidal stability. In the revised manuscript we also include orthogonal Ag-loading quantification, expanded matrix-effect and batch-reproducibility data, and a broader literature comparison to position the current platform within the rapidly growing field of label-free SERS miRNA sensing. Specifically, we aimed to:

Develop a robust, scalable chemical synthesis protocol for Ag/GO nanocomposites using an in-situ reduction strategy that ensures uniform nanoparticle distribution. Conduct an exhaustive physicochemical characterization of the material using XRD, FTIR, UV-Vis, Raman, XPS, SEM, TEM, BET, TGA, and Zeta potential analysis to understand the structure-property relationships.

Optimize the SERS performance using Rhodamine 6G (R6G) as a probe molecule to calculate enhancement factors. Demonstrate the ultrasensitive detection of miRNA-21, determining the Limit of Detection (LOD) and linearity of response.

Evaluate the specificity of the sensor against mismatched sequences and non-target miRNAs (let-7a, miR-141) and assess its performance in simulated biological fluids.Benchmark the analytical performance against representative label-free SERS miRNA assays, related Ag/GO substrates, and the practical workflow of qRT-PCR-based analysis.The resulting study links controllable Ag loading to structure-dependent SERS performance while maintaining a clinically relevant emphasis on matrix tolerance, reproducibility, and practical translation.

2. Materials and Methods

2.1. Reagents and Materials

Graphene oxide (GO) was prepared in-house from natural graphite flakes (325 mesh) using a modified Hummers

10.57647/jnsc.2026.1604.18

oxidation route, followed by extensive washing to near-neutral pH and freeze-drying. Synthetic oligonucleotides were purchased from Sangon Biotech (Shanghai, China) with HPLC purification. The sequences used for analytical validation were:

Target miRNA-21: 5'-UAG CUU AUC AGA CUG AUG UUG A-3'.12

Single-base Mismatch (mut-miR-21): 5'-UAG CUU AUC AGA CUG AUG UUG C-3'.

Non-target let-7a: 5'-UGA GGU AGU AGG UUG UAU AGU U-3'.

Non-target miR-141: 5'-UAA CAC UGU CUG GUA AAG AUG G-3'.

Homologous miR-21-3p: 5'-CAA CAC CAG UCG AUG GGC UGU-3'.

All aqueous solutions were prepared with ultrapure water, and RNase-free water was used for all miRNA handling. Commercial pooled human serum was thawed on ice immediately before use and processed as described in Section 2.3.

2.2. Synthesis of Ag/GO Nanocomposites

Ag/GO nanocomposites were prepared by in-situ chemical reduction on preformed GO sheets. Three AgNO3 loadings were intentionally selected to span a sparse-loading regime, an intermediate regime expected to maximize interparticle nanogaps, and an overgrowth regime prone to particle coalescence.

Briefly, 50 mg GO powder was dispersed in 100 mL deionized water and sonicated at 40 kHz / 300 W for 1 h to obtain a stable suspension of exfoliated sheets.

Fresh 0.1 M AgNO3 was then added dropwise in volumes of 1.0 mL, 3.0 mL, and 5.0 mL to generate Ag/GO-1, Ag/GO-2, and Ag/GO-3, respectively. After 30 min stirring at room temperature, 10 mL of 1 wt% trisodium citrate was introduced as a weak stabilizer to moderate particle growth. The suspension was heated to 90 °C under vigorous stirring, and 2.0 mL of freshly prepared 0.1 M NaBH4 was introduced dropwise. The reaction was maintained at 90 °C for 1 h, after which the solids were collected by centrifugation (8000 rpm, 10 min), washed three times with water/ethanol, and vacuum-dried at 60 °C for 12 h. For orthogonal quantification of Ag loading, dried samples were digested in dilute nitric acid and analyzed by ICP-MS. The measured Ag contents were 14.8 ± 0.6 wt% (Ag/GO-1), 35.6 ± 0.9 wt% (Ag/GO-2), and 48.7 ± 1.1 wt% (Ag/GO-3), closely matching the TGA-based estimates.

2.3. SERS Measurement Protocol

SERS measurements were performed with a Horiba LabRAM HR Evolution spectrometer coupled to an Olympus BX41 microscope.

Substrate preparation: a 10 μL aliquot of Ag/GO dispersion (1 mg/mL) was drop-cast onto a cleaned silicon wafer and dried at room temperature to form a uniform sensing film.

Analyte deposition: for R6G optimization, 10 μL of analyte solution (10^{-6} to 10^{-13} M) was deposited and dried. For serum experiments, pooled human serum was thawed on ice, centrifuged at 8000 x g for 10 min to remove debris, diluted to the indicated serum fraction (1:10, 1:2, or undiluted), spiked with synthetic miRNA, equilibrated for 15 min, and then deposited as a 10 μL droplet.

Acquisition parameters were selected after a preliminary power screen and kept constant throughout the comparative measurements.

Laser wavelength: 532 nm, selected because it overlaps the Ag/GO-2 plasmon band while preserving a strong and stable Raman response.

Laser power: 0.5 mW at the sample surface. A power screen from 0.25 to 2.0 mW showed lower signal-to-noise at 0.25 mW and progressive intensity drift / band broadening above 1.0 mW, indicating that 0.5 mW provided the best compromise between sensitivity and RNA integrity.

Objective lens: 50x long-working-distance objective (NA = 0.50), chosen to provide a reproducible sampling area and efficient signal collection. Unless otherwise noted, spectra were collected with 10 s integration time and three accumulations.

For multivariate analysis, spectra were baseline-corrected, vector-normalized, and mean-centered over the 600-1800 cm^{-1} region. PCA was performed on 126 spectra (seven classes x 18 spectra) comprising miR-21, mut-miR-21, miR-21-3p, let-7a, miR-141, BSA, and blank measurements.

3. Results and Discussion

3.1. Structural and Morphological Characterization

The crystalline nature and phase purity of the synthesized GO and Ag/GO nanocomposites were elucidated through XRD analysis. The diffraction patterns reveal distinct structural transformations occurring during the synthesis process.

As shown in Fig. 1a, the XRD pattern of pristine graphite typically shows a sharp peak at 2theta approximately 26 degrees, corresponding to the (002) plane with an interlayer spacing of about 0.34 nm [24]. After oxidation, this graphite peak vanishes and is replaced by a low-angle (001) reflection near 10.4 degrees, which is a hallmark of graphene oxide formation [25]. Applying Bragg's law, the calculated d-spacing for GO expands to approximately 0.85 nm. Such expansion is widely attributed to the insertion of oxygen-containing groups and interlayer water between oxidized carbon

10.57647/jnsc.2026.1604.18

sheets [26]. A heterogeneous but oxygen-rich GO framework containing hydroxyl, epoxide, carbonyl, and carboxyl functionalities is consistent with this behavior [27].

In the diffractograms of the Ag/GO nanocomposites, the sharp GO peak at 10.4° completely disappears. This phenomenon is indicative of the exfoliation of the GO sheets and the prevention of their restacking. The intercalation of silver nanoparticles between the layers acts as a "spacer," maintaining the separation of the sheets.

At the same time, new and clear diffraction peaks appeared at 2θ values 38.1°, 44.3°, 64.5° and 77.4°. These peaks are fully in line with the (111), (200), (220) and (311) surfaces of the face-centered cube (fcc) crystal structure of metallic silver (JCPDS card number 04-0783).

The grain size of silver nanoparticles is estimated by using the Debye-Scherrer equation:

$$D = K\lambda/\beta\cos\theta$$

In the formula, D is the crystal size, K is the shape factor (0.9), λ is the x-ray wavelength (0.15406 nm), β is the full width of the diffraction peak half-peak (FWHM) (in radiance), and θ is the Bragg angle.

The data (Table 1) reveals a trend of increasing crystallite size with higher silver precursor concentrations (Ag/GO-3). This suggests that at higher concentrations, the rate of crystal growth dominates over nucleation, or that aggregation of smaller crystallites occurs. Importantly, no peaks corresponding to silver oxide (Ag_2O) or other impurities were detected, confirming the high purity of the metallic silver and the efficacy of the reduction protocol.

Importantly, the TGA-derived loading trend was confirmed by ICP-MS, which yielded 14.8, 35.6, and 48.7 wt% Ag for Ag/GO-1, Ag/GO-2, and Ag/GO-3, respectively. This agreement supports the conclusion that the intermediate-loading sample provides substantial metallic content without the excessive coalescence observed at the highest precursor level. Ultraviolet-visible (UV-Vis) spectroscopy was used to probe both the electronic structure of GO and the plasmonic behavior of the Ag domains (Fig. 1b). Pristine GO displayed the expected absorption near 230 nm, assigned to pi-pi* transitions of aromatic C=C domains [25], together with a weaker shoulder near 300 nm from n-pi* transitions of carbonyl-containing groups. After Ag deposition, the carbon-related band red-shifted toward approximately 260 nm, consistent with partial restoration of conjugation during reduction and hybrid formation [28].

In addition, a broad Ag plasmon band emerged between 400 and 430 nm. The SPR maximum appeared at about 410 nm for Ag/GO-1, 418 nm for Ag/GO-2, and 425 nm for Ag/GO-3, with the highest-loading sample showing clear broadening. This red-shift / broadening trend is consistent with larger particles and stronger near-field coupling at higher Ag loading, whereas the intermediate-loading sample preserves strong coupling without pronounced overaggregation.

Table 1. Crystallite parameters derived from XRD analysis

Sample ID	Ag (111) Position (2θ)	FWHM (radians)	Crystallite Size (nm)	Lattice Constant (Å)
Ag/GO-1	38.08	0.0084	16.8	4.086
Ag/GO-2	38.12	0.0076	18.5	4.085
Ag/GO-3	38.15	0.0069	20.4	4.084

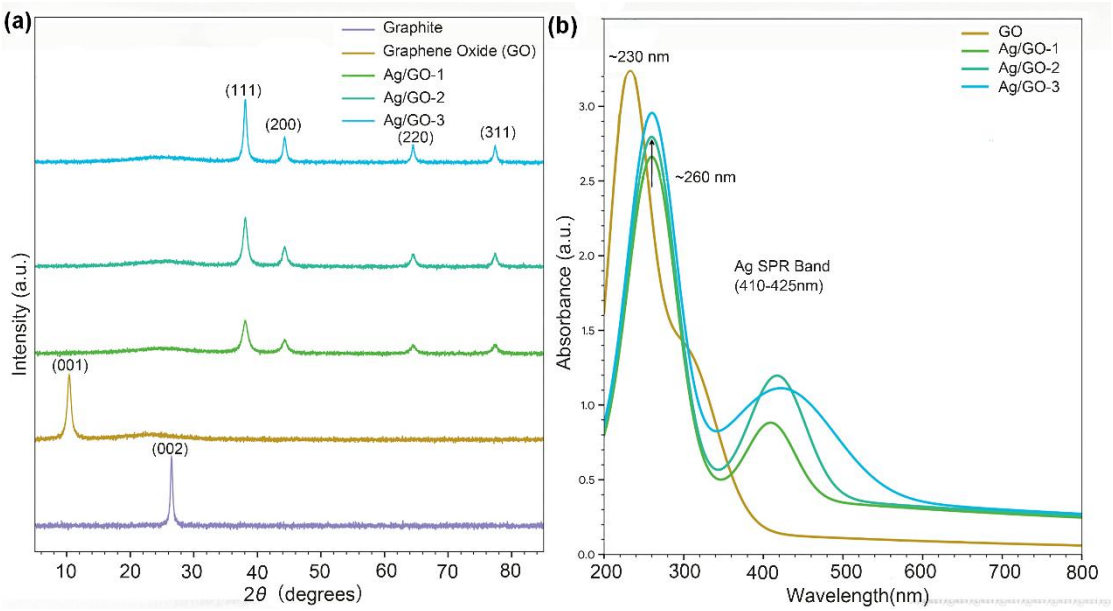

Figure 1. (a) Stacked XRD patterns of graphite, GO, and Ag/GO nanocomposites. (b) UV-Vis spectra showing the GO band shift and the emergence of the Ag plasmon band

10.57647/jnsc.2026.1604.18

FTIR analysis was used to track the evolution of oxygenated groups during Ag deposition (Fig. 2a). GO displayed broad O-H stretching near 3420 cm^{-1}, C=O stretching around 1725 cm^{-1}, a band near 1620 cm^{-1} associated with graphitic skeletal vibration / adsorbed-water bending, and a dominant C-O stretching band near 1050 cm^{-1} attributable mainly to alkoxy-type groups, which is in line with commonly reported GO vibrational signatures [24]. Notably, a distinct epoxide asymmetric-stretching band near approximately 1220 cm^{-1} was not resolved in the present spectra; we therefore avoid assigning the 1050 cm^{-1} feature to epoxide groups. After Ag deposition and borohydride reduction, the oxygen-related bands decreased markedly, confirming partial removal of oxygen functionalities and partial restoration of the graphene network [28]. At the same time, residual O-H / carboxylate features remained detectable, indicating that a fraction of surface groups was preserved to anchor Ag species and stabilize the hybrid interface.

After Ag deposition and borohydride reduction, the oxygen-related bands decreased markedly, confirming partial removal of oxygen functionalities and partial restoration of the graphene network. At the same time, residual O-H / carboxylate features remained detectable, indicating that a fraction of surface groups was preserved to anchor Ag species and stabilize the hybrid interface.

Raman spectroscopy further probed structural disorder in GO and Ag/GO (Fig. 2b). The spectra were dominated by the D band near 1350 cm^{-1}, arising from defect-activated breathing of sp^2 carbon rings, and the G band near 1590 cm^{-1}, corresponding to in-plane stretching of sp^2 carbon pairs. The ID/IG ratio is therefore used as a semi-quantitative descriptor of defect density and domain size. Quantitatively, the ID/IG ratio increases from approximately 0.92 for GO to about 1.15 for the Ag/GO-2 nanocomposite, reflecting a notable change in the carbon lattice upon chemical modification and nanoparticle incorporation. The D and G assignments used here are consistent with graphene Raman studies [29]. In graphitic materials, D/G evolution is commonly interpreted against domain-size and disorder models [30]. For graphene-derived materials, however, reduction can increase ID/IG because large oxidized domains fragment into smaller sp^2 islands even while overall conjugation improves [28].

More recent Raman analyses of GO further caution that the apparent G envelope contains contributions not captured by a single-ratio interpretation alone [31]. Moreover, the embedded AgNPs can induce a localized surface-enhanced Raman scattering effect on the graphene substrate itself. Because silver nanoparticles preferentially nucleate at defect-rich sites with higher surface energy, the local plasmonic field can selectively amplify vibrational modes associated with these regions, leading to an apparent enhancement of the D band [32].

This combined structural and plasmonic effect supports the intimate Ag-carbon contact needed to assist chemical enhancement in SERS. XPS was employed to elucidate the surface elemental composition and chemical states of the Ag/GO nanocomposite, owing to its intrinsic surface sensitivity and quantitative capability [33]. As shown in the XPS survey spectrum of Ag/GO-2 (Fig. 3a), distinct photoelectron peaks corresponding to C 1s, O 1s, and Ag 3d are clearly observed, confirming the successful incorporation of silver into the graphene-based matrix. A comparison of high-resolution C 1s spectra before and after Ag loading reveals pronounced chemical evolution (Fig. 3b).

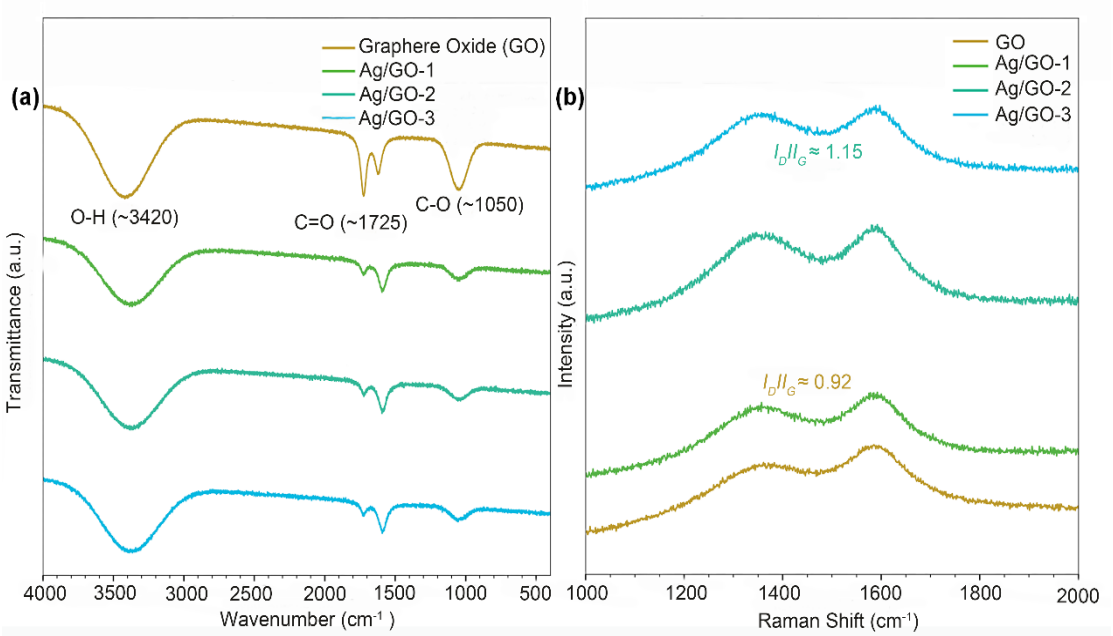

Figure 2. (a) FTIR spectra of GO and Ag/GO nanocomposites. (b) Raman spectra of GO and Ag/GO nanocomposites

10.57647/jnsc.2026.1604.18

For pristine GO, the C 1s envelope can be reliably deconvoluted into four characteristic components centered at approximately 284.8 eV (C–C/C=C, sp^2 carbon), 286.8 eV (C–O, hydroxyl/epoxy groups), 287.8 eV (C=O, carbonyl groups), and 289.0 eV (O–C=O, carboxyl groups). In contrast, the Ag/GO nanocomposite exhibits a marked decrease in the relative intensity and integrated area of oxygen-containing carbon species (C–O, C=O, and O–C=O) with respect to the graphitic C–C/C=C component. This change provides compelling evidence that graphene oxide undergoes partial chemical reduction during the Ag nanoparticle deposition process, leading to restoration of the conjugated sp^2 carbon network and enhanced electronic conductivity of the graphene scaffold.

The chemical state of silver was further examined using high-resolution Ag 3d XPS (Fig. 3c), which is critical for understanding the electronic and plasmonic properties of the composite. The Ag 3d spectrum exhibits a well-defined spin-orbit doublet with binding energies located at 368.2 eV (Ag $3d_{5/2}$) and 374.2 eV (Ag $3d_{3/2}$), corresponding to a spin-orbit splitting of 6.0 eV. These values are characteristic of metallic silver (Ag^0) rather than oxidized Ag species. Notably, silver oxides typically show a negative binding-energy shift and/or additional satellite features, none of which are detected here. The dominance of Ag^0 confirms that the deposited silver nanoparticles retain a metallic electronic structure, which is essential for localized surface plasmon resonance activity. Furthermore, a subtle negative shift of approximately 0.2 eV relative to bulk metallic silver is commonly reported for Ag-carbon hybrid systems and can be attributed to interfacial electron transfer between Ag nanoparticles and graphene sheets, driven by Fermi-level equilibration [34]. Related Ag-rGO SERS studies have similarly associated tuned defect density and interfacial coupling with stronger charge-transfer contributions [35]. Quantitative elemental analysis derived from the survey spectrum is summarized in Table 2, further confirming the successful formation of the Ag/GO composite with metallic silver uniformly distributed on the reduced graphene oxide surface.

From a SERS standpoint, the graphene component is not merely a passive support. Early studies showed that graphene itself can provide measurable Raman enhancement through chemical interactions [36]. Subsequent mechanistic work attributed this behavior to charge-transfer coupling between the adsorbate and the graphene electronic structure [37]. In Ag-rGO hybrid systems, additional photo-induced charge-transfer pathways can emerge when defect states and metal contacts are properly tuned [35].

The surface and nanoscale morphology of the Ag/GO substrates was examined by FESEM and TEM to clarify how Ag loading influences particle distribution on the GO scaffold. The wrinkled GO sheets (Fig. 4a) preserved a high accessible surface area and provided abundant anchoring sites for in-situ Ag growth (Fig. 4b). Bright, quasi-spherical Ag nanoparticles were distributed over the sheets rather than forming isolated colloidal aggregates in solution, indicating that the sheet-supported growth strategy is effective.

Further insight into nanoparticle size, spacing, and crystallinity was obtained from TEM / SAED (Fig. 4c).

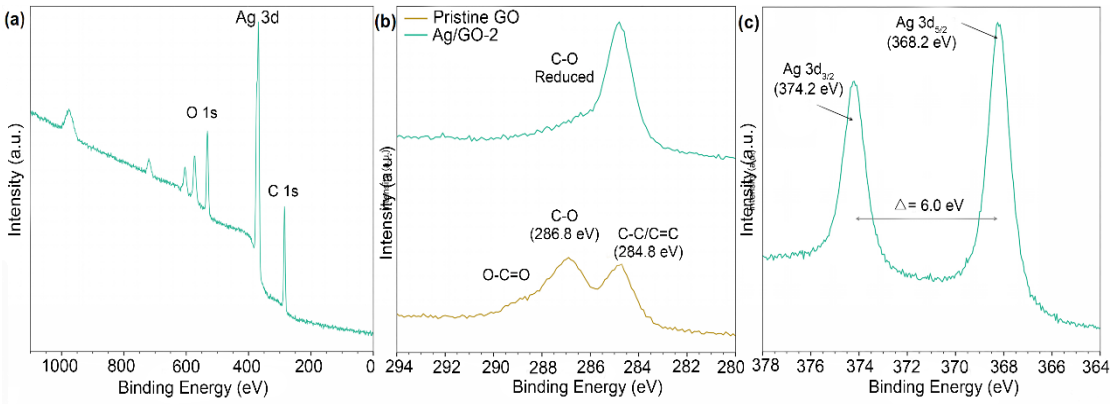

Figure 3. XPS analysis of GO and Ag/GO-2. (a) Survey spectrum. (b) High-resolution C 1s spectra of GO and Ag/GO-2. (c) High-resolution Ag 3d spectrum of Ag/GO-2

Table 2. XPS-derived elemental composition and binding energy assignments for the Ag/GO-2 nanocomposite, indicating the chemical states of carbon, oxygen, and silver

Element	Orbital	Binding Energy (eV)	Atomic % (Ag/GO-2)	Chemical State
Carbon	C 1s	284.8	62.5	C-C (sp^2)
		286.5	10.2	C-O
Oxygen	O 1s	532.1	22.4	C=O / C-OH
Silver	Ag $3d_{5/2}$	368.2	4.9	Ag^0

10.57647/jnsc.2026.1604.18

Ag/GO-1 contained relatively sparse particles of about 15 nm (Fig. 4d). Ag/GO-2 showed a higher particle density with an average diameter near 18 nm and numerous neighboring particles separated by narrow gaps, often below 5 nm in representative TEM fields. Such tight junctions are the geometric regime most often associated with strong plasmonic hot spots in nanostructured SERS systems [38]. This electromagnetic picture underpins the classical description of surface-enhanced spectroscopy [39]. Single-molecule SERS studies have further shown that dimers and similarly confined junctions can dominate the local enhancement landscape [40]. By contrast, Ag/GO-3 exhibited pronounced coalescence into >40 nm clusters, a morphology that can generate isolated hot spots but compromises uniformity and repeatability.

The textural properties of GO and Ag/GO-2 were evaluated by N_2 adsorption-desorption and BJH pore analysis (Fig. 5). Both samples showed type IV isotherms with H3 hysteresis, consistent with slit-like mesopores formed by stacked sheet-like domains. GO exhibited a surface area of approximately 450 m^2 g^{-1}, whereas Ag/GO-2 retained ~180 m^2 g^{-1} after Ag deposition and partial reduction. BJH analysis indicated a broad mesopore distribution centered in the low-nanometer range with a pore volume of about 0.32 cm^3 g^{-1}, suggesting that Ag/GO-2 preserves analyte-accessible mesoporosity even after substantial metal loading. TGA showed the expected suppression of oxygen-group decomposition after reduction, while the residual mass at 800 °C corresponded to an Ag content of ~36 wt% for Ag/GO-2. Importantly, ICP-MS yielded 35.6 wt% Ag for the same sample, supporting the reliability of the loading estimate.

Zeta-potential analysis confirmed that GO remained strongly anionic at neutral pH, while Ag/GO-2 retained a moderately negative surface charge sufficient for suspension stability. This balance between reduced oxygen content and preserved surface charge is favorable because it improves conductivity and interfacial coupling without causing rapid aggregation before film formation.

3.2. SERS Performance Evaluation

Rhodamine 6G (R6G) was used as a model probe molecule to evaluate the intrinsic SERS activity of the Ag/GO substrates because it provides a well-defined Raman fingerprint (Fig. 6a). Characteristic bands were observed near 612 cm^{-1}, 774 cm^{-1}, 1361 cm^{-1}, and 1650 cm^{-1}, and their intensity varied strongly with Ag loading. Ag/GO-1 produced relatively weak signals because the particle density was too low to create a dense electromagnetic network, whereas Ag/GO-3 suffered from overaggregation and reduced uniformity.

Ag/GO-2 gave the strongest and most reproducible response, consistent with its intermediate particle size and spacing.

To quantify the SERS performance of Ag/GO-2, a concentration-dependent study of R6G was performed over several orders of magnitude (Fig. 6b). The 1361 cm^{-1} band remained detectable down to 10^{-11} M, and the calculated enhancement factor reached 2.4 x 10^7.

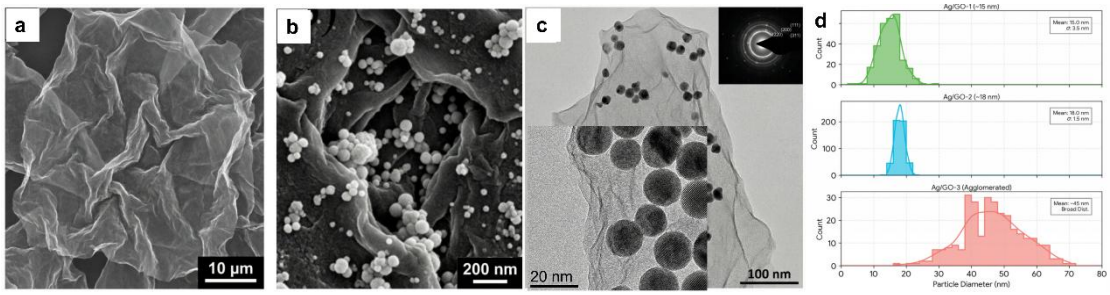

Figure 4. FESEM and TEM characterization of GO and Ag/GO substrates. (a) Low-magnification FESEM image. (b) High-magnification FESEM image of Ag/GO-2. (c) TEM image and SAED pattern of Ag/GO-2. (d) Particle-size distributions for Ag/GO-1, Ag/GO-2, and Ag/GO-3

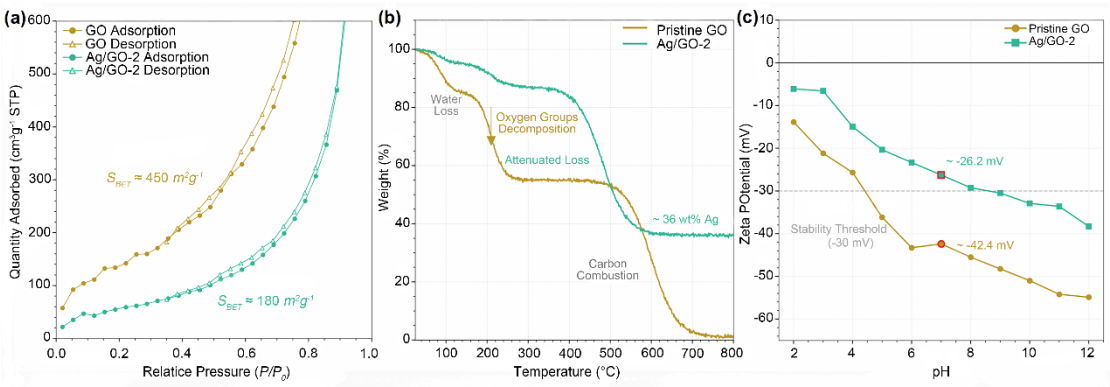

Figure 5. Textural and colloidal characterization of GO and Ag/GO-2. (a) N_2 adsorption-desorption / pore-distribution analysis. (b) TGA curves. (c) Zeta potential as a function of pH

10.57647/jnsc.2026.1604.18

This value is consistent with strong hotspot formation at the optimized intermediate Ag loading and is comparable to graphene-silver substrates optimized through controlled metal loading [41]. Related rGO/Ag platforms have likewise demonstrated that homogeneity, stability, and analyte affinity must be balanced rather than maximized independently [42].

Pyramid-array hybrids that combine graphene oxide with multiscale plasmonic junctions point to the same general design principle [43]. These conclusions are also in line with more recent Ag/GO composite reports [22] and related GO/Ag substrates [23]. We emphasize, however, that neither nanogap-mediated electromagnetic enhancement nor GO-assisted charge transfer is proven by a single experiment here; rather, these mechanisms are inferred collectively from TEM gap statistics, optical absorption behavior, XPS evidence of interfacial electronic coupling, and the observed enhancement trend across the loading series.

Beyond simple dye sensing, several graphene-assisted SERS architectures underscore why Ag/GO-2 performs best at intermediate loading. Molecularly imprinted GO-Ag hybrid films illustrate how interfacial recognition can raise selectivity without abandoning graphene-mediated enhancement [44]. Durable GO-Ag nanocomposites further show that GO can slow the loss of silver activity during storage [45].

GO/Ag composites optimized for l-theanine detection confirm that well-dispersed nanoparticles on GO create more accessible hot spots [46]. Ag/rGO nanosheets have also been used as SERS platforms for trace uranyl sensing [47]. More recent membrane-based formats report that structural uniformity is closely tied to reproducibility [48]. A 2024 GO-coated metallic nanotube array reached strong linearity and low-RSD response by imposing a highly ordered plasmonic geometry [49].

3.3. Label-Free Detection of miRNA-21

As shown in Fig. 7 and Table 3, the central function of the developed SERS platform is the direct, label-free identification of miRNA-21 on Ag/GO-2. In contrast to R6G, nucleic acids rely primarily on the intrinsic polarizability of their purine and pyrimidine bases, and adenine-rich modes are often among the most SERS-active features on silver surfaces [50]. The spectrum of miRNA-21 showed a distinct set of nucleobase and backbone features absent from the blank substrate. Considering the polarization selection rules of SERS, the observed pattern is more consistent with tilted or mixed adsorption geometries than with a purely flat orientation of the heterocyclic bases on the Ag surface [51].

Among these features, the band centered at approximately 732 cm^{-1} was especially prominent and was assigned to the adenine ring-breathing mode, consistent with classical SERS studies of nucleic-acid bases on Ag surfaces [50]. The use of adenine-dominated bands as endogenous label-free markers has also been highlighted in SERS-based nucleic-acid hybridization studies [51]. Because miRNA-21 contains multiple adenine residues, this band was selected as the primary quantitative marker. Additional bands around 650, 795, 1090, 1245, and 1480-1580 cm^{-1} enriched the sequence fingerprint and enabled comparison with homologous and non-target controls at the full-spectrum level rather than through a single intensity ratio alone.

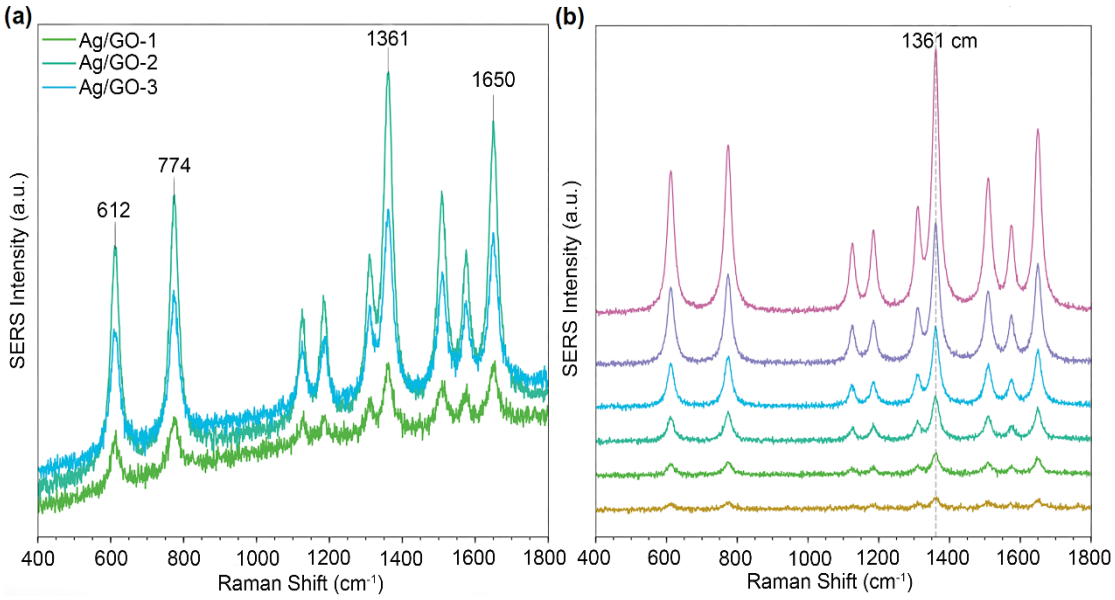

Figure 6. SERS performance of Ag/GO substrates using R6G. (a) Comparative spectra on Ag/GO-1, Ag/GO-2, and Ag/GO-3. (b) Concentration-dependent spectra on Ag/GO-2 used for EF estimation

10.57647/jnsc.2026.1604.18

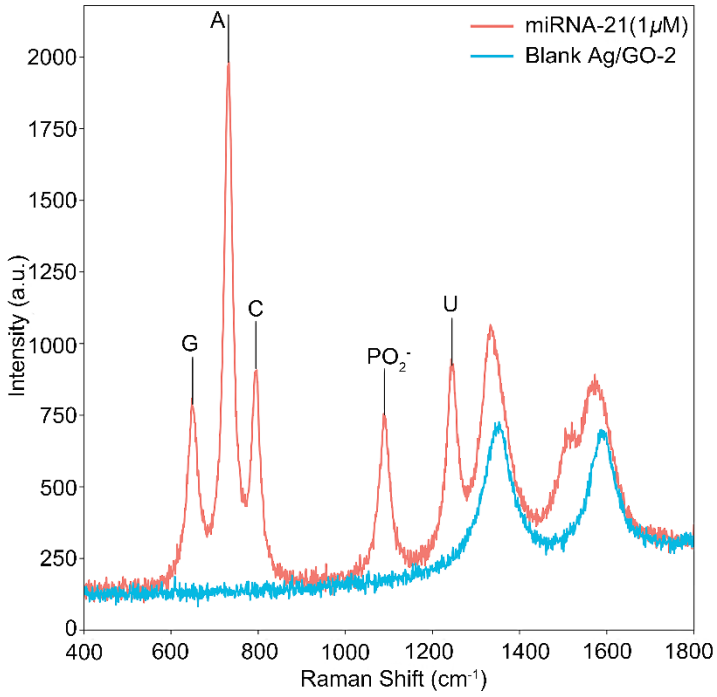

Figure 7. Label-free SERS spectrum of miRNA-21 acquired on Ag/GO-2 compared with the blank Ag/GO-2 surface

Table 3. Assigned SERS peak positions and corresponding vibrational modes for miRNA-21 on Ag/GO-2, including nucleobase ring-breathing and stretching vibrations (adenine, guanine, cytosine, uracil) and the PO_2^- symmetric stretching band of the phosphate backbone

Peak Position (cm−1)	Assignment	Origin
732	Ring breathing mode	Adenine (A)
650	Ring breathing mode	Guanine (G)
795	Ring breathing mode	Cytosine (C)
1245	Ring stretching / C-N	Uracil (U)
1330	C-N stretch	Adenine
1090	PO_2^- symmetric stretch	Phosphate Backbone
1480-1580	C=C / C=N stretch	In-plane Ring modes

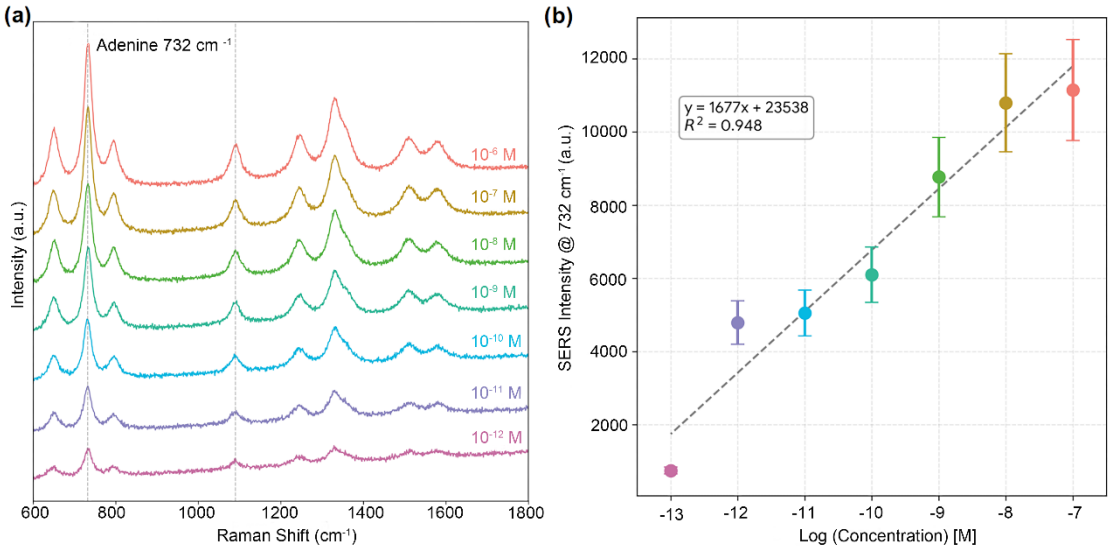

Figure 8. Sensitivity and calibration of the miRNA-21 assay on Ag/GO-2. (a) Stacked SERS spectra from 1 μM to 10 fM. (b) Calibration plot of the 732 cm^{-1} band showing the corrected R^2 value of 0.948

The analytical sensitivity of the SERS assay toward miRNA-21 was evaluated over the range 1 μM to 10 fM on Ag/GO-2 (Fig. 8a). The adenine band at 732 cm^{-1} decreased monotonically with concentration, and a linear

10.57647/jnsc.2026.1604.18

calibration was obtained from 10^{-7} to 10^{-13} M with R^2 = 0.948 (Fig. 8b). Using the 3sigma/S criterion, the limit of detection was estimated to be 15 fM. While amplification-assisted platforms can push the LOD even lower [17], the present response remains competitive with microfluidic label-free systems [18] and direct unlabeled-miRNA fingerprinting strategies [19].

Compared with representative literature, the present platform occupies a practically useful middle ground: it is less sensitive than DSN-amplified SERS assays for miR-21 [17], but it avoids enzymatic signal amplification and maintains a simpler substrate-based workflow. Relative to microfluidic label-free systems [18], the current approach sacrifices device integration in favor of easier fabrication. Compared with direct unlabeled miRNA fingerprinting on Ag nanostructures [19], the Ag/GO scaffold provides improved robustness in serum-like matrices. Recent Ag/GO reports have highlighted the importance of balancing sensitivity and stability in optimized Ag/GO composites [22]. Related GO/Ag substrates point to similar structure-performance trade-offs [23], and the revised data indicate that Ag/GO-2 reaches this balance through intermediate Ag loading, preserved mesoporosity, and acceptable batch reproducibility.

Selectivity and specificity were evaluated by comparing miR-21 with a single-base mismatch (mut-miR-21), the closely related miR-21-3p sequence, two non-target lung-cancer-associated miRNAs (let-7a and miR-141), and BSA (Fig. 9). All miRNA sequences shared adenine-derived bands near 732 cm^{-1}, but the full spectral fingerprints differed in the 650-800, 1090, and 1200-1400 cm^{-1} regions because of their distinct base composition and stacking interactions on the Ag/GO surface. BSA produced only weak features in the nucleobase fingerprint window, consistent with lower effective adsorption / enhancement for globular proteins on this substrate.

To move beyond single-peak metrics, PCA was applied to the full spectral data set. The analysis used 126 spectra (seven classes x 18 spectra) after baseline correction and vector normalization over the 600-1800 cm^{-1} window. The first two principal components captured the majority of the variance and produced well-separated clusters for miR-21, mut-miR-21, miR-21-3p, let-7a, miR-141, BSA, and blank measurements. This multivariate separation confirms that the platform can discriminate target and interferent classes from the complete spectral pattern rather than from a single diagnostic peak.

The practical applicability of solid SERS substrates depends on both spatial uniformity and temporal stability. Twenty random spots on a single Ag/GO-2 substrate gave a 12.4% RSD for the 732 cm^{-1} signal, indicating good spot-to-spot homogeneity (Fig. 10). To assess batch reproducibility, three independently prepared Ag/GO-2 batches were evaluated at 1 pM miR-21, yielding an inter-batch RSD of 10.8%. Long-term stability was examined by storing the dried substrates in the dark in sealed Petri dishes at 25 ± 2 °C and 45 ± 5% relative humidity. After 30 days, the substrates retained more than 85% of their initial activity, consistent with partial GO-mediated passivation of the Ag surface.

The analytical performance of the platform in a biologically relevant environment was examined by spiking miR-21 into human serum (Table 4). In 1:10 diluted serum, recoveries remained between 92.0% and 108.0% with RSD values from 5.4% to 11.2%. A more stringent dilution series at fixed 1 pM target level showed that the normalized 732 cm^{-1} response retained 85.0% recovery in 1:2 serum and 76.0% recovery in undiluted serum, with RSD values below 16%. These trends are consistent with protein-corona formation and competitive adsorption in protein-rich media [52].

More broadly, nanoparticle-protein interactions in physiological environments are known to redefine the effective surface presented to biomolecules [53]. Even so, the characteristic nucleobase bands remained identifiable, indicating that the GO-supported substrate preserves partial anti-biofouling resilience even at elevated serum content.

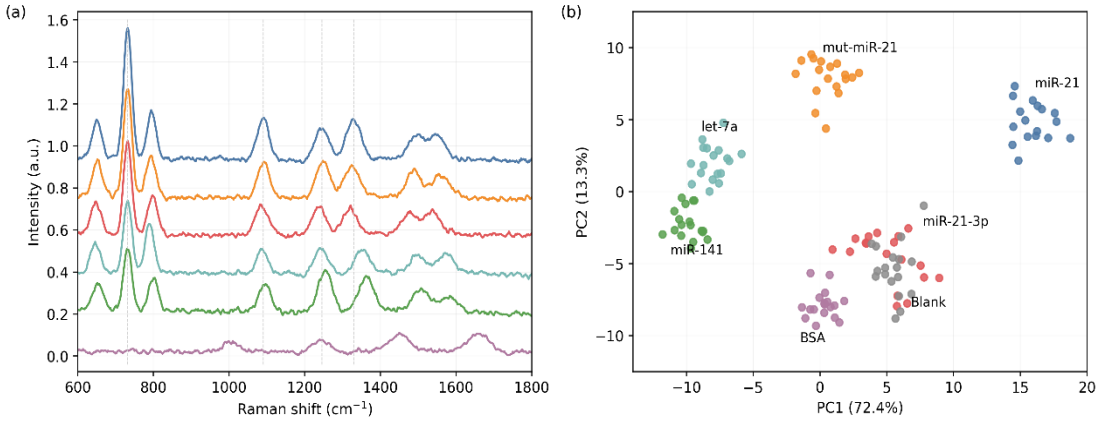

Figure 9. Specificity analysis of the Ag/GO-2 assay. (a) Full spectral of miR-21, mut-miR-21, miR-21-3p, let-7a, miR-141, and BSA. (b) Multi-class PCA score plot based on the full spectral data set

10.57647/jnsc.2026.1604.18

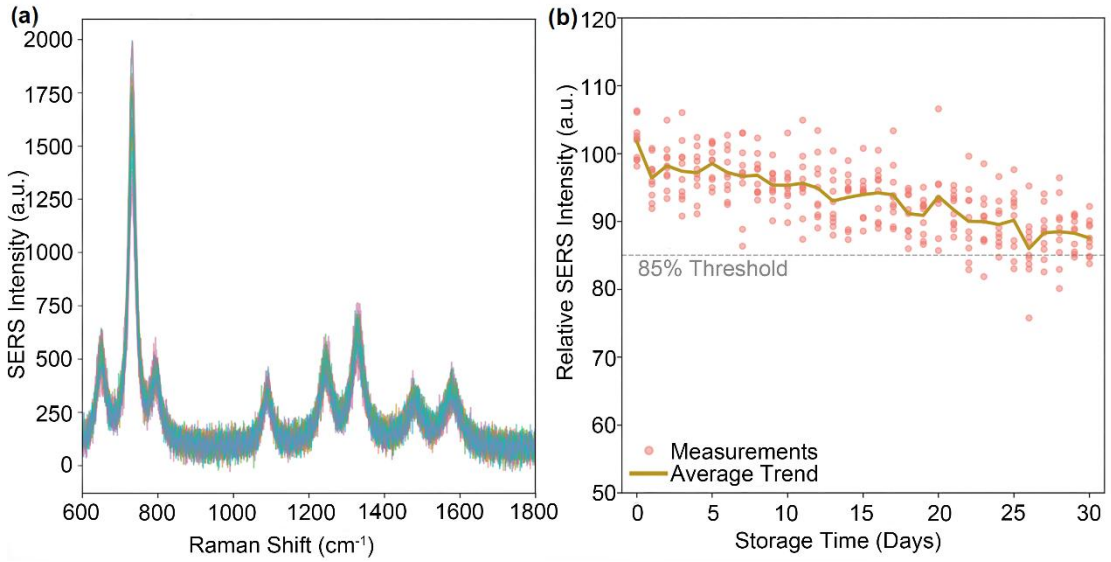

Figure 10. Reproducibility and stability of Ag/GO-2. (a) Spectra collected from 20 random spots with the corresponding 732 cm^{-1} RSD. (b) Time-dependent signal retention during 30-day dark sealed storage

Table 4. Recovery of miR-21 in diluted and concentrated human-serum matrices using the Ag/GO-2 SERS sensor

Matrix	Spiked Concentration	Recovered Concentration	Recovery (%)	RSD (n=3)
Serum (1:10)	10 nM	9.50 nM	95.0	5.4%
Serum (1:10)	1 pM	0.92 pM	92.0	8.5%
Serum (1:10)	100 fM	108 fM	108.0	11.2%
Serum (1:2)	1 pM	0.85 pM	85.0	13.7%
Serum (undiluted)	1 pM	0.76 pM	76.0	15.9%

Table 5. Qualitative comparison of the present assay with representative miRNA detection strategies

Method	Assay design	Amplification	Representative feature	Practical implication
RT-qPCR	Reverse transcription + quantitative PCR	Yes	High analytical sensitivity but multistep workflow	Reference method; higher reagent and instrument burden
Novara et al. 2017 [52]	Optofluidic SERS chip for label-free miRNA analysis	No enzymatic amplification	Microfluidic quantitative detection	Integrated format but more elaborate device functionalization
Li et al. 2020 [53]	Direct SERS fingerprinting of unlabeled miRNA	No	Demonstrated direct miRNA spectral readout on Ag nanostructures	Strong fingerprint capability; limited matrix discussion
Yao et al. 2021 [51]	Iodide-modified AgNPs + DSN cycling for miR-21	Yes	Ultrahigh sensitivity through enzymatic signal amplification	Higher sensitivity but greater workflow complexity
This work	Ag/GO drop-cast substrate for direct miR-21 detection	No	15 fM LOD, serum applicability, batch reproducibility	Balanced simplicity, selectivity, and robustness

For practical benchmarking, the present platform should be viewed against both label-free SERS literature and amplification-based reference workflows. Compared with qRT-PCR, the Ag/GO assay avoids reverse transcription, primers, and thermal cycling, while compared with recent SERS reports it offers a simpler substrate-driven format with meaningful serum tolerance (Table 5). Recent integrated miRNA platforms illustrate the trade-off between analytical performance and operational simplicity. A DNAzyme-assisted SERS-microfluidic system improved quantitative performance through reciprocal amplification and device integration [54]. A dual-mode SERS/electrochemical interface similarly increased signal redundancy, but required more

elaborate interfacial assembly and exonuclease-mediated transduction [55]. In this context, the present Ag/GO assay prioritizes direct spectral readout, simple fabrication, and acceptable performance in serum-rich media.

4. Conclusion

In this work, we demonstrated the rational design and analytical use of an ultrasensitive Ag/GO nanocomposite for label-free detection of lung cancer-associated miRNA-21. The revised analysis shows that intermediate Ag loading is critical because it balances particle density, nanogap formation, mesoporosity, and surface stability. Ag/GO-2 combined an average Ag crystallite size of ~18.5 nm, ~35.6 wt% Ag loading, preserved mesoporosity, and strong hotspot-mediated enhancement, enabling a 15 fM detection limit without fluorescent labels, capture probes, or enzymatic amplification. The platform further showed sequence-level discrimination against homologous and non-target controls, acceptable batch reproducibility, retention of >85% activity after 30 days, and measurable responses in both diluted and concentrated serum matrices. Although additional validation in whole blood and clinical patient cohorts will be needed, the revised data support Ag/GO as a practical route toward simple SERS-based liquid-biopsy analysis. Future microfluidic integration will require careful control of substrate adhesion, channel wetting, flow-induced delamination, residence time, and nonspecific fouling to preserve hotspot accessibility under continuous operation.

Ethical approval
This study did not involve human participants, animal experiments, or identifiable clinical specimens. Commercial pooled human serum was used only as an analytical matrix for method validation; therefore, institutional ethics approval was not required.

Competing interest
The authors state that no conflicts of interest exist in relation to this study.

Data availability
The datasets generated and analyzed in this study will be provided upon reasonable request.

References

[1] Zhou, J.; Xu, Y.; Liu, J.; Feng, L.; Yu, J.; Chen, D. Global Burden of Lung Cancer in 2022 and Projections to 2050: Incidence and Mortality Estimates from GLOBOCAN. *Cancer Epidemiol.* **93**, 102693 (2024).

[2] Ying, L.; Lu, T.; Tian, Y.; Guo, H.; Wu, C.; Xu, C.; Jin, J.; Zhu, R.; Liu, P.; Yang, Y.; et al. A Predictive Model for Prognostic Risk Stratification of Early-Stage NSCLC Based on Clinicopathological and miRNA Panel. *Lung Cancer* **195**, 107902 (2024).

[3] Rodriguez-Manzano, J.; Subramaniam, S.; Uchea, C.; Szostak-Lipowicz, K. M.; Freeman, J.; Rauch, M.; Tinto, H.; Zar, H. J.; D'Alessandro, U.; Holmes, A. H.; et al. Innovative Diagnostic Technologies: Navigating Regulatory Frameworks through Advances, Challenges, and Future Prospects. *Lancet Digit. Health* **6**, e934–e943 (2024).

[4] Alharbi, T. A. F.; Rababa, M.; Alsuwayl, H.; Alsubail, A.; Alenizi, W. S. Diagnostic Challenges and Patient Safety: The Critical Role of Accuracy—A Systematic Review. *J. Multidiscip. Healthc.* **18**, 3051–3064 (2025).

[5] Wang, X.; Chen, Y.; Ma, C.; Bi, L.; Su, Z.; Li, W.; Wang, Z. Current Advances and Future Prospects of Blood-Based Techniques for Identifying Benign and Malignant Pulmonary Nodules. *Crit. Rev. Oncol. Hematol.* **207**, 104608 (2025).

[6] Lazaros, K.; Adam, S.; Krokidis, M. G.; Exarchos, T.; Vlamos, P.; Vrahatis, A. G. Non-Invasive Biomarkers in the Era of Big Data and Machine Learning. *Sensors* **25**, 1396 (2025).

[7] Silvia Lima, R. Q. da; Vasconcelos, C. F. M.; Gomes, J. P. A.; Bezerra de Menezes, E. da S.; de Oliveira Silva, B.; Montenegro, C.; Paiva Júnior, S. de S. L.; Pereira, M. C. miRNA-21, an oncomiR That Regulates Cell Proliferation, Migration, Invasion and Therapy Response in Lung Cancer. *Pathol. Res. Pract.* **263**, 155601 (2024).

[8] Chen, L.; Liu, S.; Tao, Y. Regulating Tumor Suppressor Genes: Post-Translational Modifications. *Signal Transduct. Target. Ther.* **5**, 90 (2020).

[9] Priyadarsini, S.; Mohanty, S.; Mukherjee, S.; Basu, S.; Mishra, M. Graphene and Graphene Oxide as Nanomaterials for Medicine and Biology Application. *J. Nanostruct. Chem.* **8**, 123–137 (2018).

[10] Hosseini, F.; Dadmehr, M. Optical Biosensors for miRNA Detection: Lighting the Path to Cancer Diagnosis. *Sensing and Bio-Sensing Research* **52**, 101008 (2026).

[11] Zhao, S.; Fernald, R. D. Comprehensive Algorithm for Quantitative Real-Time Polymerase Chain Reaction. *J. Comput. Biol.* **12**, 1047–1064 (2005).

[12] Bong, D.; Sohn, J.; Lee, S.-J. V. Brief Guide to RT-qPCR. *Mol. Cells* **47**, 100141 (2024).

[13] Han, X. X.; Rodriguez, R. S.; Haynes, C. L.; Ozaki, Y.; Zhao, B. Surface-Enhanced Raman Spectroscopy. *Nat. Rev. Methods Primers* **1**, 87 (2022).

[14] Hu, C.; Guan, M.; Mi, F.; Zhang, S.; Geng, P. Multimodal SERS Biosensing Platforms: Emerging Opportunities for Ultrasensitive Biomarker Detection and Intelligent Diagnostics. *ACS Sensors* **11**, 1794–1830 (2026).

[15] Wei, H.; Xu, H. Hot Spots in Different Metal Nanostructures for Plasmon-Enhanced Raman Spectroscopy. *Nanoscale* **5**, 10794–10805 (2013).

[16] Maher, R. C. SERS Hot Spots. In *Raman Spectroscopy for Nanomaterials Characterization*; Kumar, C. S. S. R., Ed.; Springer: Berlin, Heidelberg, pp 215–260 (2012).

[17] John, A.; Benny, L.; Cherian, A. R.; Narahari, S. Y.; Varghese, A.; Hegde, G. Electrochemical Sensors Using Conducting Polymer/Noble Metal Nanoparticle Nanocomposites for the Detection of Various Analytes: A Review. *J. Nanostruct. Chem.* **11**, 1–31 (2021).

[18] Novara, C.; Chiado, A.; Paccotti, N.; Catuogno, S.; Esposito, C. L.; Condorelli, G.; De Franciscis, V.; Geobaldo, F.; Rivolo, P.; Giorgis, F. SERS-Active Metal-Dielectric Nanostructures Integrated in Microfluidic Devices for Label-Free Quantitative Detection of miRNA. *Faraday Discuss.* **205**, 271–289 (2017).

[19] Li, D.; Xia, L.; Zhou, Q.; Wang, L.; Chen, D.; Gao, X.; Li, Y. Label-Free Detection of miRNA Using Surface-Enhanced Raman Spectroscopy. *Anal. Chem.* **92**, 12769–12773 (2020).

[20] Sun, M.; Li, J. Graphene Oxide Membranes: Functional Structures, Preparation and Environmental Applications. *Nano Today* **20**, 121–137 (2018).

[21] Chaudhry, I.; Hu, G.; Ye, H.; Jensen, L. Toward Modeling the Complexity of the Chemical Mechanism in SERS. *ACS Nano* **18**, 20835–20850 (2024).

[22] He, T.; Xiong, S.; Han, H.; Wang, D.; Wang, Y.; Dai, C.; Liu, W. Facile Synthesis of Ag/GO SERS Composite with Highly Sensitive and Stable Performance. *Colloids Surf. A Physicochem. Eng. Asp.* **662**, 131008 (2023).

[23] Olar, G. C.; Cotet, L. C.; Baia, L.; Mihis, A.; Baia, M. SERS-Active Substrates Based on Graphene Oxide or Reduced Graphene Oxide and Silver Nanoparticles. *Mater. Today Proc.* **45**, 4096–4099 (2021).

[24] Dreyer, D. R.; Park, S.; Bielawski, C. W.; Ruoff, R. S. The Chemistry of Graphene Oxide. *Chem. Soc. Rev.* **39**, 228–240 (2010).

[25] Stankovich, S.; Dikin, D. A.; Piner, R. D.; Kohlhaas, K. A.; Kleinhammes, A.; Jia, Y.; Wu, Y.; Nguyen, S. T.; Ruoff, R. S. Synthesis of Graphene-Based Nanosheets via Chemical Reduction of Exfoliated Graphite Oxide. *Carbon* **45**, 1558–1565 (2007).

[26] Kueh, T. C.; Chew, S. H.; Soh, A. K.; Hung, Y. M. Investigation of the Influence of the Location of Oxygenated Functional Groups in Graphene Nanostructures on Water Permeation via Molecular Dynamics Simulations. *Appl. Surf. Sci.* **609**, 155414 (2023).

[27] Dreyer, D. R.; Todd, A. D.; Bielawski, C. W. Harnessing the Chemistry of Graphene Oxide. *Chem. Soc. Rev.* **43**, 5288–5301 (2014).

[28] Pei, S.; Cheng, H.-M. The Reduction of Graphene Oxide. *Carbon* **50**, 3210–3228 (2012).

[29] Ferrari, A. C.; Meyer, J. C.; Scardaci, V.; Casiraghi, C.; Lazzeri, M.; Mauri, F.; Piscanec, S.; Jiang, D.; Novoselov, K. S.; Roth, S.; Geim, A. K. Raman Spectrum of Graphene and Graphene Layers. *Phys. Rev. Lett.* **97**, 187401 (2006).

[30] Tuinstra, F.; Koenig, J. L. Raman Spectrum of Graphite. *J. Chem. Phys.* **53**, 1126–1130 (1970).

[31] King, A. A. K.; Davies, B. R.; Noorbehesht, N.; Newman, P.; Church, T. L.; Harris, A. T.; Razal, J. M.; Minett, A. I. A New Raman Metric for the Characterisation of Graphene Oxide and Its Derivatives. *Sci. Rep.* **6**, 19491 (2016).

[32] Campos, A.; Troc, N.; Cottancin, E.; Pellarin, M.; Weissker, H.-C.; Lermé, J.; Kociak, M.; Hillenkamp, M. Plasmonic Quantum Size Effects in Silver Nanoparticles Are Dominated by Interfaces and Local Environments. *Nat. Phys.* **15**, 275–280 (2019).

[33] Cui, Y.; Liao, Y.; Sun, Y.; Wang, W.; Wu, J.; Dai, W.; Huang, T. Advanced XPS-Based Techniques in the Characterization of Catalytic Materials: A Mini-Review. *Catalysts* **14**, 595 (2024).

[34] Liu, M.; Yang, W.; Xiao, R.; Li, J.; Tan, R.; Qin, Y.; Bai, Y.; Zheng, L.; Hu, L.; Gu, W.; et al. Lattice Atom-Bridged Chemical Bond Interface Facilitates Charge Transfer for Boosted Photoelectric Response. *Natl. Sci. Rev.* **12**, nwae465 (2025).

[35] Guo, S.; Jin, S.; Park, E.; Chen, L.; Mao, Z.; Jung, Y. M. Photo-Induced Charge Transfer Enhancement for SERS in a SiO_2-Ag-Reduced Graphene Oxide System. *ACS Appl. Mater. Interfaces* **13**, 5699–5705 (2021).

[36] Ling, X.; Xie, L.; Fang, Y.; Xu, H.; Zhang, H.; Kong, J.; Dresselhaus, M. S.; Zhang, J.; Liu, Z. Can Graphene Be Used as a Substrate for Raman Enhancement? *Nano Lett.* **10**, 553–561 (2010).

[37] Ling, X.; Moura, L. G.; Pimenta, M. A.; Zhang, J. Charge-Transfer Mechanism in Graphene-Enhanced Raman Scattering. *J. Phys. Chem. C* **116**, 25112–25118 (2012).

[38] Ding, S.-Y.; Yi, J.; Li, J.-F.; Ren, B.; Wu, D.-Y.; Panneerselvam, R.; Tian, Z.-Q. Nanostructure-Based Plasmon-Enhanced Raman Spectroscopy for Surface Analysis of Materials. *Nat. Rev. Mater.* **1**, 16021 (2016).

[39] Moskovits, M. Surface-Enhanced Spectroscopy. *Rev. Mod. Phys.* **57**, 783–826 (1985).

[40] Camden, J. P.; Dieringer, J. A.; Wang, Y.; Masiello, D. J.; Marks, L. D.; Schatz, G. C.; Van Duyne, R. P. Probing the Structure of Single-Molecule Surface-Enhanced Raman Scattering Hot Spots. *J. Am. Chem. Soc.* **130**, 12616–12617 (2008).

[41] Ding, G.; Xie, S.; Liu, Y.; Wang, L.; Xu, F. Graphene Oxide-Silver Nanocomposite as SERS Substrate for Dye Detection: Effects of Silver Loading Amount and Composite Dosage. *Appl. Surf. Sci.* **345**, 310–318 (2015).

[42] Naqvi, T. K.; Srivastava, A. K.; Kulkarni, M. M.; Siddiqui, A. M.; Dwivedi, P. K. Silver Nanoparticles Decorated Reduced Graphene Oxide (rGO) SERS Sensor for Multiple Analytes. *Appl. Surf. Sci.* **478**, 887–895 (2019).

[43] Li, Z.; Xu, S. C.; Zhang, C.; Liu, X. Y.; Gao, S. S.; Hu, L. T.; Guo, J.; Ma, Y.; Jiang, S. Z.; Si, H. P. High-Performance SERS Substrate Based on Hybrid Structure of Graphene Oxide/AgNPs/Cu Film@Pyramid Si. *Sci. Rep.* **6**, 38539 (2016).

[44] Jiang, Y.; Carboni, D.; Malfatti, L.; Innocenzi, P. Graphene Oxide-Silver Nanoparticles in Molecularly-Imprinted Hybrid Films Enabling SERS Selective Sensing. *Materials* **11**, 1674 (2018).

[45] Jiang, Y.; Wang, J.; Malfatti, L.; Carboni, D.; Senes, N.; Innocenzi, P. Highly Durable Graphene-Mediated Surface Enhanced Raman Scattering (G-SERS) Nanocomposites for Molecular Detection. *Appl. Surf. Sci.* **450**, 451–460 (2018).

[46] Zheng, H.; Ni, D.; Yu, Z.; Liang, P. Preparation of SERS-Active Substrates Based on Graphene Oxide/Silver Nanocomposites for Rapid Detection of L-Theanine. *Food Chem.* **217**, 511–516 (2017).

[47] Dutta, S.; Ray, C.; Sarkar, S.; Pradhan, M.; Negishi, Y.; Pal, T. Silver Nanoparticle Decorated Reduced Graphene Oxide (rGO) Nanosheet: A Platform for SERS-Based Low-Level Detection of Uranyl Ion. *ACS Appl. Mater. Interfaces* **5**, 8724–8732 (2013).

[48] Celik, Y.; Akcil, B.; Aksoy, E. SERS Performance of Silver Nanoparticle/Reduced Graphene Oxide-Coated Filter Membranes. *Fullerenes Nanotubes Carbon Nanostruct.* **31**, 833–844 (2023).

[49] Chang, T.-H.; Tseng, C.-Y.; Altama, A. K.; Yiu, P.; Chu, J. P. Graphene Oxide-Coated Metallic Nanotube Array as a Surface-Enhanced Raman Scattering (SERS) Substrate. *Vacuum* **226**, 113320 (2024).

[50] Koglin, E.; Sequaris, J.-M.; Valenta, P. Surface Enhanced Raman Spectroscopy of Nucleic Acid Bases on Ag Electrodes. *J. Mol. Struct.* **79**, 185–189 (1982).

[51] Barhoumi, A.; Halas, N. J. Label-Free Detection of DNA Hybridization Using Surface Enhanced Raman Spectroscopy. *J. Am. Chem. Soc.* **132**, 12792–12793 (2010).

[52] Walczyk, D.; Baldelli Bombelli, F.; Monopoli, M. P.; Lynch, I.; Dawson, K. A. What the Cell "Sees" in Bionanoscience. *J. Am. Chem. Soc.* **132**, 5761–5768 (2010).

[53] Walkey, C. D.; Chan, W. C. W. Understanding and Controlling the Interaction of Nanomaterials with Proteins in a Physiological Environment. *Chem. Soc. Rev.* **41**, 2780–2799 (2012).

[54] Ma, L.; Ye, S.; Wang, X.; Zhang, J. SERS-Microfluidic Approach for the Quantitative Detection of miRNA Using DNAzyme-Mediated Reciprocal Signal Amplification. *ACS Sens.* **6**, 1392–1399 (2021).

[55] He, C.; Hu, Y.; Qi, H.; Li, P.; Yuan, R.; Yang, X. SERS-Electrochemical Dual-Mode Detection of MicroRNA on Same Interface Assisted by Exonuclease III Signal Transformation. *Anal. Chim. Acta* **1293**, 342286 (2024).

10.57647/jnsc.2026.1604.18